

Thermodynamics and Kinetics in Antibody Resistance of the 501Y.V2 SARS-CoV-2 Variant

Son Tung Ngo,^{ab*} Trung Hai Nguyen,^{ab} Duc-Hung Pham,^c and Nguyen Thanh Tung,^{de} Pham Cam Nam,^{f*}

^aLaboratory of Theoretical and Computational Biophysics, Ton Duc Thang University, Ho Chi Minh City 700000, Vietnam

^bFaculty of Applied Sciences, Ton Duc Thang University, Ho Chi Minh City 700000, Vietnam

^cDivision of Immunobiology, Cincinnati Children's Hospital Medical Center, Cincinnati 45229, OH, USA

^dInstitute of Materials Science, Vietnam Academy of Science and Technology, Hanoi 100000, Vietnam

^eGraduate University of Science and Technology, Vietnam Academy of Science and Technology, Hanoi 100000, Vietnam

^fDepartment of Chemical Engineering, The University of Da Nang, University of Science and Technology, Da Nang City 550000, Vietnam

ABSTRACT: Understanding thermodynamics and kinetics of the binding process of an antibody to SARS-CoV-2 receptor-binding domain (RBD) of Spike protein is very important for the development of COVID19 vaccines. Especially, it is essential to understand how the binding mechanism may change under the effects of RBD mutations. In this context, we have demonstrated that the South African variant (B.1.351 or 501Y.V2) can resist the neutralizing antibody (NAb). Three substitutions in RBD including K417N, E484K, and N501Y alters the free energy landscape, binding pose, binding free energy, binding kinetics, and unbinding pathway of RBD + NAb complexes. The low binding affinity of NAb to 501Y.V2 RBD confirms the antibody resistance of the South African variant.

INTRODUCTION

The novel β -coronavirus, SARS-CoV-2, whose sequence is similar to SARS-CoV-1 and MERS-CoV inducing human respiratory epidemic in the beginning of this century, is the cause of the human respiratory disease (COVID-19) pandemic worldwide.^{1, 2} This virus has been infecting more than 100 million cases and associated with more than 2 million deaths. SARS-CoV-2 is a single-positive-strand RNA virus, whose genome encodes for four main components: spike, envelope, membrane and nucleocapsid.^{3, 4} The spike protein (protein S) of SARS-CoV-2 which is used by the virus to bind to human angiotensin-converting-enzyme 2 (ACE2), has been researched thoroughly. ACE2 is present in different tissues in the body, including the lung, heart and liver,⁵ is employed by SARS-CoV-2 as receptor to bind and infect human cells. The S trimer comprises three copies of S₁ and S₂ subunits. S₁ subunit contains 4 domains: S_{1A}, S_{1B}, S_{1C} and S_{1D}, in which S_{1B} domain is also called receptor-binding

domain (RBD), which mediates the attachment of spike protein to target cell via binding to ACE2 receptor.⁶ Once RBD is in the 'up' conformation, it can recognize and bind into ACE2, which leads to the conformational changes of S₂ subunit and enables SARS-CoV-2 to fuse with cell membrane and to enter host cells.^{1, 6}

RBD is the main target of neutralizing antibodies (NAbs) which can be isolated from plasma of COVID-19 patients, immunoglobulin libraries, or immunized laboratory animal models.¹ These NAbs can be roughly divided into four main classes, of which class 1s' and class 2s' RBD epitopes overlap with the ACE2-binding site, suggesting a neutralization mechanism that involves direct competition with ACE2. Class 1 antibodies, which are encoded by the immunoglobulin V-gene (VH3-53) segment with complementarity-determining regions 1 and 2 (CDRH₁ and CDRH₂) and a short CDRH₃, are mostly elicited by SARS-CoV-2 infection. On the other hand, when class 2 antibodies also target site I10,15 which is also target epitopes of class 1 antibodies, they bind to RBD in both 'up' and 'down' conformations of S protein.^{1, 7} Additionally, class 3 antibodies bind outside ACE2 and recognize both up and down RBD, while class 4 antibodies comprise previously described antibodies that cannot block ACE2 and target only to RBD in 'up' conformation.¹ Besides RBD, the N-terminal domain (NTD) of protein S is also a popular target for NAbs and many potent monoclonal antibodies directed against this region show great potential in clinical trials for COVID-19 treatment.⁷ The majority of these antibodies target a single immunodominant site on NTD, including the N1-loop (NTD N-terminus), N3-loop (supersite b-hairpin), and N5 loop (supersite loop). Subsets of these antibodies and NAbs in class 1 and class 3 form multi-donor classes, with different set of VH germline restricted mode of spike recognition.⁷

MATERIALS & METHODS

The three-dimensional structure of SARS-CoV-2 RBD and their antibodies NAb/fNAb was found from the Protein Data Bank (PDB) with the identities of 7BWJ.¹³ The resolution of 7BWJ and 2.85 Å. Moreover, as mentioned above, it should be noted that the new variant of the SARS-CoV-2 in South Africa, B.1.351 or 501Y.V2, forms eight changes in the Spike protein. There are four substitutions and a deletion in the N-terminal domain (NTD) including L18F, D80A, D215G, Δ242-244, and R246I. Consequently, three substitutions were found in RBD involving K417N, E484K, and N501Y. The RBD structure with three substitutions was thus prepared via changing three residues of 7BWJ using the PyMOL mutagen tools.¹⁴

The atomistic simulation was performed using the GROMACS version 5.1.5 with general-purpose computing on graphics processing units.¹⁵ The protein, antibody, and neutralized ions were parameterized via the Amber99SB-ILDN force field¹⁶ since it is one of the most suitable force fields for free energy calculation.^{17, 18} The TIP3P water model was chosen to simulate the water molecule.¹⁹ The systemic

The MD simulation parameters were referred to the previous works.^{20, 21} However, in particular, the integral was efforded every 3 femtoseconds. A non-bonded pair between two atoms were affected within a radius of 0.9 nm, in which the electrostatic interaction was calculated using the fast Particle-Mesh Ewald electrostatics approach²² as well as the van der Waals (vdW) interaction was computed using the cut-off scheme. The solvated complex was initially optimized using the energetic minimization simulation via the steepest descent method. The minimized system was then relaxed in NVT and NPT ensembles with a length of 100 ps each simulation. During NVT and NPT simulations, the integral was attempted every 1 femtosecond. The equilibrium snapshots obtained via NPT simulations were used as starting conformations of MD simulations. The conventional MD simulations were performed with interval 100 ns and repeated 4 times independently.

Steered-MD simulation. Representative structures of RBD + NAb systems, which were obtained via MD simulations, were employed as initial shapes of FPL simulations. The complexes were reinserted into the rectangular PBC box for

saving the computing resources. The configuration information was described in Figure 1C-D and Table S1. The FPL simulations were carried out to generate unbinding conformations of the systems, which were used as starting shapes of US simulations. From the beginning, the NABs were forced to dissociate from the binding mode with the WT/501Y.V2 RBD using SMD simulations. In particular, eight SMD trajectories were carried out to probe the most optimal-unbinding pathway. The trajectory, in which the rupture force, F_{Max} , and pulling work, W , formed the smallest deviation in comparison with the median values, was used for generating US windows. In FPL, the NAB was pulled along Z-axis via an external force using cantilever $k = 1000 \text{ kJ mol}^{-1} \text{ nm}^{-2}$ and constant velocity $v = 0.001 \text{ nm ps}^{-1}$. During the simulation, the RBD was softly fixed via C_{α} restrain. The pulling force, NAb displacement, and systemic coordinates were recorded every 33 integrated steps.

Umbrella sampling simulation. The systemic snapshots, which were extracted from the FPL trajectory since the NAB displaced every ca. 1.0 \AA along the unbinding pathway ξ , were used as starting shapes of US simulations. Ca. 25 US windows each complex were simulated with a length of 10 ns of MD simulation to calculate the potential of mean force (PMF) curve. It should be noted that a short NPT simulation was executed to reduce initial fluctuations.^{23, 24} The PMF values were calculated via the weighted histogram analysis method (WHAM).²⁵ The free energy barriers, $\Delta G_{\text{on}}^{++}$ and $\Delta G_{\text{off}}^{++}$, and binding free energy, ΔG_{b} , of the binding process between RBD and NAb were estimated as described as Figure 1E.

Analyzed Tools

The free energy landscape (FEL) of the complex was constructed using the principal component analysis (PCA) method.²⁶ A non-bonded contact was counted when the pair between two atoms is smaller than 4.5 \AA . The PMF value was estimated via the Weighted Histogram Analysis Method (WHAM) with the execution of auto-correlated time. The computed error was calculated using the bootstrapping method.²⁷

RESULTS AND DISCUSSION

It should be noted that investigating structures of protein-protein complexes and understanding how they bind

together are fundamental issues.²⁸ Moreover, structures of several complexes remain difficult to estimate experimentally.^{29, 30} Furthermore, in order to characterize the protein-protein binding mechanisms is required powerful experimental approaches,^{31, 32} but the obtained data are normally limited or indirect. Obtaining direct data at an atomic level about binding pathways and physical insights into the binding mechanisms are still open issues.²⁸ Atomistic MD simulations emerge as potential approaches for investigating both dynamics and structural change of protein-protein complexes. Using MD simulations, we can easily monitor the associate and dissociate processes of a monomer to the others.^{21, 33} However, in fact, the association of two proteins consumes a long time more than the simulation timescale. Normally, the enhanced sampling methods, which may combine several short simulation trajectories, are used to modeling the unbinding process of two proteins. The association of protein-protein is thus predicted. Therefore, in this work, atomistic simulations will be performed to reveal the insights at the atomic level of the binding process of an antibody to various SARS-CoV-2 variants RBD. Structural changes of the SARS-CoV-2 RBD + antibody complexes were characterized via MD simulations. Thermodynamics and kinetics of the binding process were then revealed via a combination of SMD and US simulations. The obtained results probably enhance the vaccine developments.

Unbiased MD simulations were carried out to understand the structural change at the atomistic level of 501Y.V2 RBD + NABs since the binding affinity of the NABs to 501Y.V2 RBD was altered according to the recent report.^{7, 9, 10, 12} The stabilized conformations of the RBD + NAB complexes were investigated over the equilibrium trajectories (cf. Figure S1 of the SI file). The principal component analysis (PCA) method was employed to generate the free energy landscape (FEL) of RBD + NAB systems.²⁶ The obtained results were described in **Figure 2**. Clearly, the 501Y.V2 variant increases the number of the FEL local minima implying that the 501Y.V2 complex is more flexible than the WT one. It also shows that the binding free energy ΔG_{b} between 501Y.V2 RBD and NABs is significantly reduced.

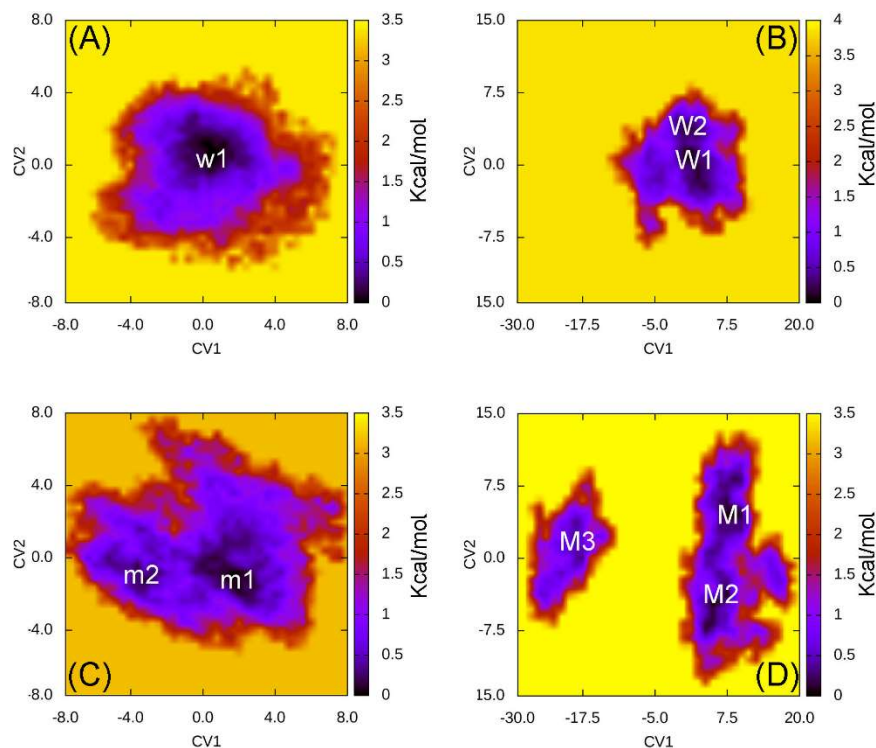


Figure 2. Free energy landscape of RBD + antibody was constructed using PCA method. In particular, (A) presents the FEL of the WT RBD + fNAb; (B) mentions the FEL of the WT RBD + NAb; (C) describes the FEL of the 501Y.V2 RBD + fNAb; and (D) denotes the FEL of the 501Y.V2 RBD + NAb.

The WT RBD + fNAb only formed one minimum noted as **w1** in **Figure 2A**, which is located at (CV1; CV2) coordinates of (0.40; 0.40). In particular, the antibody adopted HBs to 4 residues of the WT RBD including G447, Y449, N450, and E484 (cf. **Figure 3**). These results suggest that a mutation E484K will be significantly altered the binding affinity/mechanism of the RBD + fNAb. Two minima were observed in FEL of 501Y.V2 RBD + fNAb, which are located at (CV1; CV2) coordinates of (1.60; -1.40) and (-3.60; -1.00) denoted as **m1** and **m2**, respectively. Analyzing the representative structure **m1**, the antibody was found to be

able to form HBs to the residues K444, G447, Y449, and N450 of the 501Y.V2 RBD. The corresponding residues of **m2**, which formed HBs to RBD 2-4, are G447, Y449, N450, and K484 (cf. **Figure 3**). The observed structural changes imply that the binding affinity and kinetics between RBD and fNAb probably change. A similar story of RBD + NAb, which is detailed mentioned in the SI file, was obtained confirming the results.

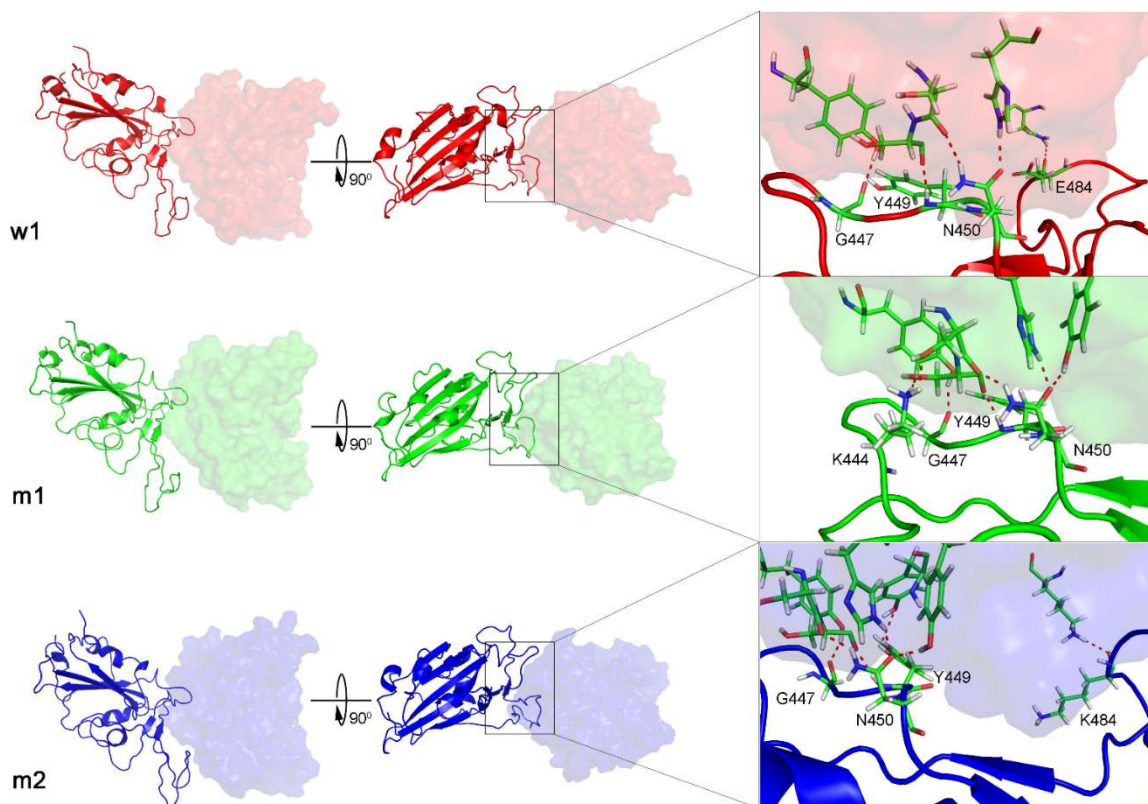


Figure 3. The representative structures of WT and 501Y.V2 RBD + fNAb in different perspective. The structures corresponds to the minima **w1**, **m1**, and **m2**.

The WT/501Y.V2 RBD + NAb systems were also investigated. FEL of the complexes was significantly altered when the mutations were induced. The WT RBD + NAb formed two minima, which were shown in **Figure 2B**. These minima located at (CV1; CV2) coordinates of (0.63; 0.75) and (0.63; 3.38) denoting as **W1** and **W2**, respectively. Besides that, the 501Y.V2 RBD + NAb FEL (**Figure 2D**) adopted three minima, which located at (CV1; CV2) coordinates of (7.50; 4.13), (5.63; -4.50), and (-18.8; 1.50) labelling as **M1**, **M2**, and **M3**, respectively. Analyzing the complex **W1**, the HBs were observed between antibody and residues G447, Y449, N450, and E484 of the RBD that is in good consistency to the **w1** case. However, HBs were only found between the NAb and residue E484 of the WT RBD in the complex **W2** (**Figure 4**). The obtained results indicate that residue E484 plays an important role in the binding process of the antibody to the RBD. Replacing the E484 with another residue probably modifies the binding mechanism of the NAb to RBD rather than substitutions at the different positions. Moreover, it should be noted that in the 501Y.V2 variant induced, a lysine residue substitutes the glutamate residue at the sequence 484. The replacement probably terminates the HBs and weakening the attracted force between the NAb and the RBD.

The argument was confirmed via evaluations of the representative structures of 501Y.V2 RBD + NAb complexes. In conformation **M1**, the HBs between NAb and the residues G447, Y449, and N450 of RBD were found. The residues G447, Y449, N450, and T470 of 501Y.V2 RBD procedure HBs to NAb in conformation **M2**. Furthermore, The NAb only found two HBs to the residue E471 and N481 of the 501Y.V2 RBD. The free energy approach should be carried out to clarify the change of binding affinity upon the structural changes of the 501Y.V2 RBD + NAb complexes.

As discussed above, the RBD + fNAb structure is more flexible when the 501Y.V2 variant was induced. The binding affinity/mechanism of the complex is thus altered. In this work, a combination of steered-molecular dynamics (SMD)/umbrella sampling (US) simulations were carried out to probe the change in RBD + NAb association. The SMD was used to generate US windows (cf. the ESI file). The free energy profile was then calculated using the WHAM.²⁵ The binding free energy ΔG_b between RBD and NAb is able to calculate via PMF curve as mentioned in **Figure 1E**.^{23, 24} Moreover, the free energy barriers ΔG_{on}^{++} and ΔG_{off}^{++} , which were associated with the binding kinetic rate constant k_{on} and the unbinding kinetic rate constant k_{off} can be also estimated, respectively.

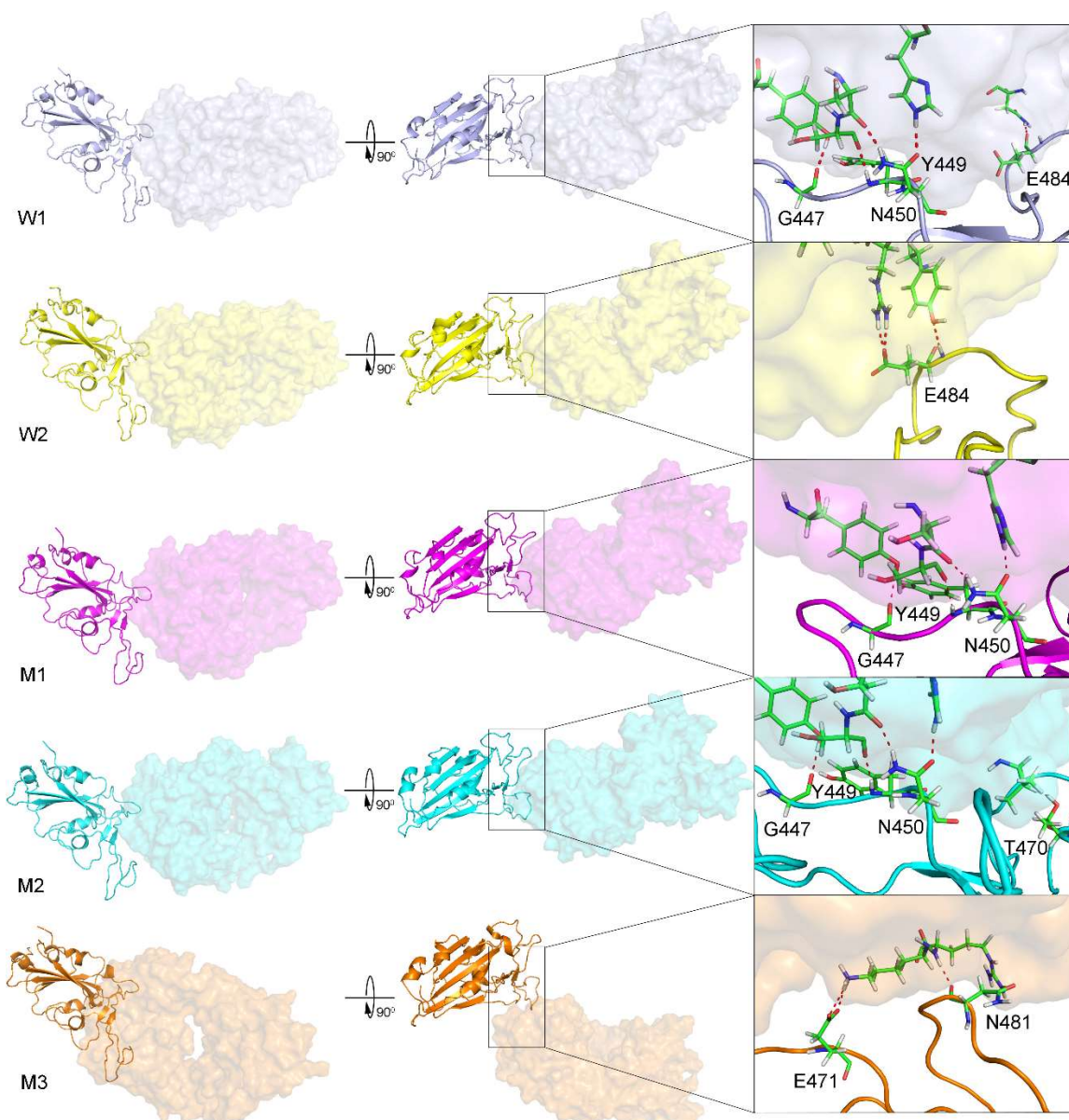


Figure 4. The representative structures of WT and 501Y.V2 RBD + NAb corresponding to the minima **W1**, **W2**, **M1**, **M2**, and **M3**. The interaction diagram between RBD and NAb were obtained using PyMOL tool.

As discussed above, the RBD + fNAb structure is more flexible when the 501Y.V2 variant was induced. The binding affinity/mechanism of the complex are thus altered. In this work, a combination of steered-molecular dynamics (SMD)/umbrella sampling (US) simulations were carried out to probe the change in RBD + NAb association. The SMD was used to generate US windows (cf. the SI file). The free energy profile was then calculated using the WHAM.²⁵ The binding free energy ΔG_b between RBD and NAb is able to calculate via PMF curve as mentioned in **Figure 1E**.^{23, 24} Moreover, the free energy barriers ΔG_{on}^{++} and ΔG_{off}^{++} , which were associated with the binding kinetic rate constant k_{on} and the unbinding kinetic rate constant k_{off} can be also estimated, respectively.

The calculated results for free energy barriers (cf. **Table 1**) indicated that the NAb will bind to 501Y.V2 RBD more

difficult than WT one because of the larger ΔG_{on}^{++} . NAb is much easier to bind to than to unbind from RBD, because the ΔG_{off}^{++} is larger than the ΔG_{on}^{++} . However, in the **M3** case, the $\Delta G_{off}^{++} = 0.14 \pm 0.18$ kcal mol⁻¹ is significantly smaller than the $\Delta G_{on}^{++} = 2.83 \pm 0.65$ kcal mol⁻¹ indicating that it takes more time for NAb to bind to 501Y.V2 RBD for them unbind. Moreover, the observations were also confirmed due to the binding free energy, ΔG_b , calculations, in which the thermodynamic metric corresponding to the association between NAb and RBD is significantly decreased when the 501Y.V2 variant was induced (**Table 1**). The NAb is thus resisted to bind to 501Y.V2 RBD. Therefore, it may be argued that the 501Y.V2 variant could reduce the vaccine efficiency. The observation is in good agreement with the experimental data.^{7, 9, 10, 12}

Table 1. The calculated results using SMD and US simulations.^a

N ^o	System	F_{Max}	W	ΔG_{on}^{++}	ΔG_{off}^{++}	ΔG_b
1	WT RBD + NAb 2-4 (w1)	1388.0 \pm 18.6	139.9 \pm 3.3	0.24 \pm 0.20	18.31 \pm 0.82	-18.07 \pm 0.84
2	501Y.V2 RBD + NAb 2-4 (m1)	859.3 \pm 40.7	72.8 \pm 3.4	0.81 \pm 0.26	12.00 \pm 0.82	-11.19 \pm 0.77
3	501Y.V2 RBD + NAb 2-4 (m2)	1007.4 \pm 31.2	86.8 \pm 3.1	0.73 \pm 0.11	11.62 \pm 0.54	-10.89 \pm 0.55
4	WT RBD + NAb (W1)	1133.6 \pm 39.0	178.8 \pm 8.5	0.36 \pm 0.75	39.82 \pm 1.31	-39.46 \pm 1.08
5	WT RBD + NAb (W2)	1137.6 \pm 25.8	181.5 \pm 6.5	0.76 \pm 0.29	43.36 \pm 0.73	-42.60 \pm 0.67
6	501Y.V2 RBD + NAb (M1)	745.5 \pm 25.4	96.1 \pm 3.6	0.62 \pm 0.15	21.64 \pm 0.66	-20.93 \pm 0.68
7	501Y.V2 RBD + NAb (M2)	748.0 \pm 33.1	81.6 \pm 6.5	0.42 \pm 0.24	16.16 \pm 0.88	-15.74 \pm 0.91
8	501Y.V2 RBD + NAb (M3)	470.2 \pm 25.7	50.5 \pm 4.5	2.83 \pm 0.65	0.14 \pm 0.18	-2.70 \pm 0.68

^aThe calculated results over SMD and US simulations. The details of free energy profile and histograms over US simulations were reported in Figure S3-S6.

The collective-variable FEL,³⁴ was constructed by number of contacts between two proteins within 0.45 nm and the displacement of the antibody, revealed the unbinding pathway of NAb. The obtained FEL was shown in **Figure 5** and Figure S2 of the SI file. The representative structures of the complexes within a backbone RMSD of 0.2 nm were then estimated using clustering method.²⁶ The unbinding pathways were significantly altered under effects of the 501Y.V2 variant. A larger number of transition states of the WT RBD + fNAb complex implies that it is hard to unbind

the antibody from WT system than 501Y.V2 variant. Moreover, the representative structures **B**, **b**, and **b'** correspond to the binding model of the RBD + fNAb complexes. The structures **D7**, **d6**, and **d4'** respond to the minima where the fNAb completely detached from RBD. The other conformations correspond to dissociated structures along unbinding pathways. The similar picture was also observed when the RBD + NAb complexes were investigated (Figure S2).

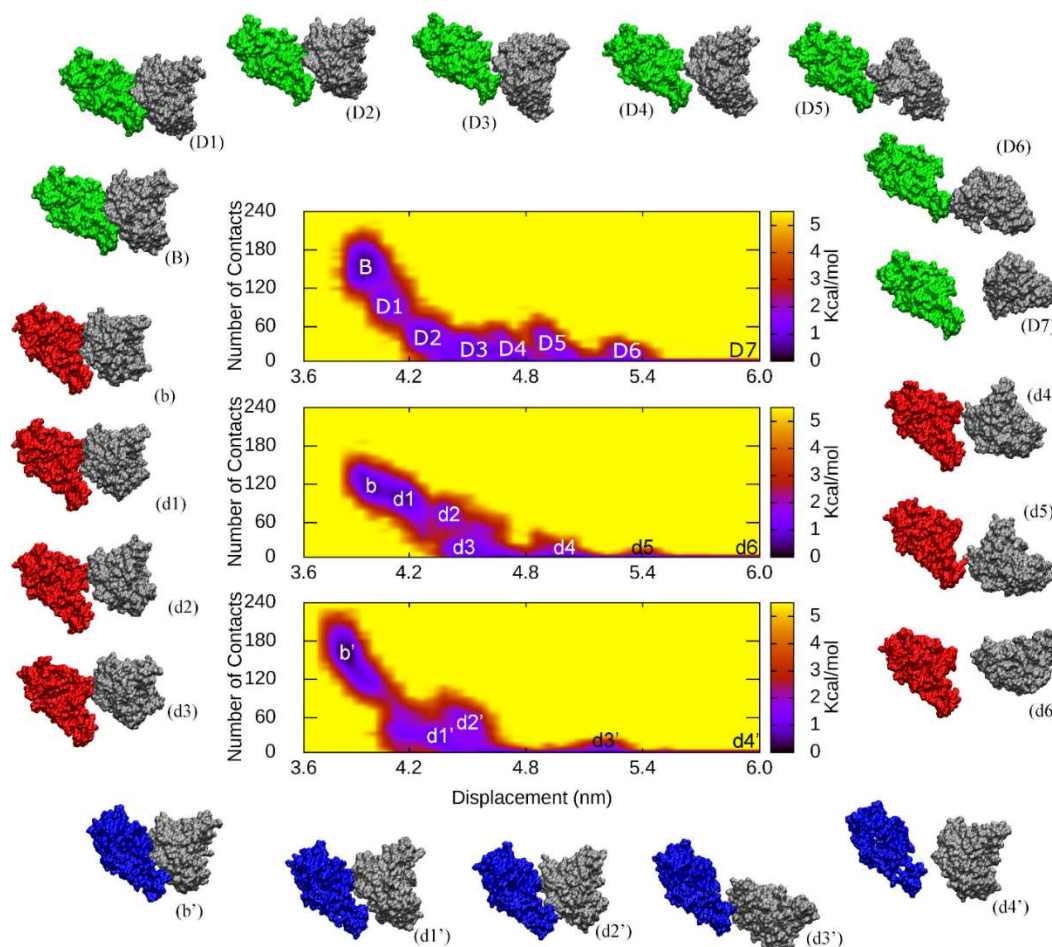


Figure 5. The collective-variable FEL revealed the unbinding pathways of fNAb from the binding mode with WT/501Y.V2 RBD. The representative structures of complexes were also estimated.

CONCLUSIONS

In this work, the NAb resistance of 501Y.V2 variant was investigated using atomistic simulations. In particular, the binding pose of NAb/fNAb to WT/501Y.V2 RBD was revealed using atomistic simulations. Increasing FEL minima of 501Y.V2 RBD + NAb/fNAb in comparison with the WT RBD systems infer that the complex 501Y.V2 RBD + NAb/fNAb is more unstable than the WT one. Thermodynamics and kinetics of the binding process between RBD and NAb were also determined using SMD/US simulations. Interestingly, the binding free energy ΔG_b of WT RBD + NAb/fNAb is significantly smaller than that of 501Y.V2 RBD + NAb/fNAb. It is consistent with results of the binding kinetic rate constant k_{on} and the unbinding kinetic rate constant k_{off} . Poorly binding affinity of NAb/fNAb to 501Y.V2 RBD confirm the antibody resistance of the South African variant.^{7, 9, 10, 12}

ASSOCIATED CONTENT

Supporting Information

Supporting Information Available: backbone RMSD of RBD + NAb systems; the collective-variable FEL revealed the unbinding pathways of NAb from the WT/501Y.V2 RBD + NAb complexes; free energy profile over the unbinding process of fNAb out of the WT/501Y.V2 RBD + fNAb complexes; the histograms of US simulations over the unbinding process of fNAb out of the WT/501Y.V2 RBD + fNAb complexes; free energy profile over the unbinding process of NAb out of the WT/501Y.V2 RBD + NAb complexes; and the histograms of US simulations over the unbinding process of NAb out of the WT/501Y.V2 RBD + NAb complexes. The material is available free of charge via the Internet at <http://pubs.acs.org>.

AUTHOR INFORMATION

Corresponding Author

*Email: ngosontung@tdtu.edu.vn and pcnam@dut.udn.vn

Author Contributions

All authors contributed to doing computations and preparing the manuscript.

Notes

The authors declare no competing financial interests.

ACKNOWLEDGMENT

This work was supported by Vietnam National Foundation for Science & Technology Development (NAFOSTED) grant #104.99-2019.57.

REFERENCES

- Barnes, C. O.; West, A. P.; Huey-Tubman, K. E.; Hoffmann, M. A. G.; Sharaf, N. G.; Hoffman, P. R.; Koranda, N.; Gristick, H. B.; Gaebler, C.; Muecksch, F.; Lorenzi, J. C. C.; Finkin, S.; Häggglöf, T.; Hurley, A.; Millard, K. G.; Weisblum, Y.; Schmidt, F.; Hatziioannou, T.; Bieniasz, P. D.; Caskey, M.; Robbani, D. F.; Nussenzweig, M. C.; Bjorkman, P. J., Structures of Human Antibodies Bound to SARS-CoV-2 Spike Reveal Common Epitopes and Recurrent Features of Antibodies. *Cell* **2020**, *182* (4), 828-842.e16.
- de Wit, E.; van Doremalen, N.; Falzarano, D.; Munster, V. J., SARS and MERS: recent insights into emerging coronaviruses. *Nature Reviews Microbiology* **2016**, *14* (8), 523-534.
- Ngo, S. T.; Quynh Anh Pham, N.; Thi Le, L.; Pham, D.-H.; Vu, V. V., Computational Determination of Potential Inhibitors of SARS-CoV-2 Main Protease. *Journal of Chemical Information and Modeling* **2020**, *60* (12), 5771-5780.
- Schoeman, D.; Fielding, B. C., Coronavirus envelope protein: current knowledge. *Virology Journal* **2019**, *16* (1), 69.
- Hoffmann, M.; Kleine-Weber, H.; Schroeder, S.; Kruger, N.; Herrler, T.; Erichsen, S.; Schiergens, T. S.; Herrler, G.; Wu, N. H.; Nitsche, A.; Muller, M. A.; Drosten, C.; Pohlmann, S., SARS-CoV-2 Cell Entry Depends on ACE2 and TMPRSS2 and Is Blocked by a Clinically Proven Protease Inhibitor. *Cell* **2020**.
- Lan, J.; Ge, J.; Yu, J.; Shan, S.; Zhou, H.; Fan, S.; Zhang, Q.; Shi, X.; Wang, Q.; Zhang, L.; Wang, X., Structure of the SARS-CoV-2 spike receptor-binding domain bound to the ACE2 receptor. *Nature* **2020**, *581* (7807), 215-220.
- Wibmer, C. K.; Ayres, F.; Hermanus, T.; Madzivhandila, M.; Kgagudi, P.; Oosthuysen, B.; Lambson, B. E.; de Oliveira, T.; Vermeulen, M.; van der Berg, K.; Rossouw, T.; Boswell, M.; Ueckermann, V.; Meiring, S.; von Gottberg, A.; Cohen, C.; Morris, L.; Bhiman, J. N.; Moore, P. L., SARS-CoV-2 501Y.V2 escapes neutralization by South African COVID-19 donor plasma. *Nature Medicine* **2021**.
- WHO, Coronavirus disease 2019 (COVID-19) Situation Report – 52. **2020**.
- Wang, P.; Nair, M. S.; Liu, L.; Iketani, S.; Luo, Y.; Guo, Y.; Wang, M.; Yu, J.; Zhang, B.; Kwong, P. D.; Graham, B. S.; Mascola, J. R.; Chang, J. Y.; Yin, M. T.; Sobieszczyk, M.; Kyrtatous, C. A.; Shapiro, L.; Sheng, Z.; Huang, Y.; Ho, D. D., Antibody Resistance of SARS-CoV-2 Variants B.1.351 and B.1.1.7. *Nature* **2021**.
- Hoffmann, M.; Arora, P.; Groß, R.; Seidel, A.; Hörnich, B. F.; Hahn, A. S.; Krüger, N.; Graichen, L.; Hofmann-Winkler, H.; Kempf, A.; Winkler, M. S.; Schulz, S.; Jäck, H.-M.; Jahrsdörfer, B.; Schrezenmeier, H.; Müller, M.; Kleger, A.; Münch, J.; Pöhlmann, S., SARS-CoV-2 Variants B.1.351 and P.1 Escape from Neutralizing Antibodies. *Cell* **2021**.
- Weisblum, Y.; Schmidt, F.; Zhang, F.; DaSilva, J.; Poston, D.; Lorenzi, J. C. C.; Muecksch, F.; Rutkowska, M.; Hoffmann, H.-H.; Michailidis, E.; Gaebler, C.; Agudelo, M.; Cho, A.; Wang, Z.; Gazumyan, A.; Cipolla, M.; Luchsinger, L.; Hillyer, C. D.; Caskey, M.; Robbani, D. F.; Rice, C. M.; Nussenzweig, M. C.; Hatziioannou, T.; Bieniasz, P. D., Escape from neutralizing antibodies by SARS-CoV-2 spike protein variants. *eLife* **2020**, *9*, e61312.
- Cele, S.; Gazy, I.; Jackson, L.; Hwa, S.-H.; Tegally, H.; Lustig, G.; Giandhari, J.; Pillay, S.; Wilkinson, E.; Naidoo, Y.; Karim, F.; Ganga, Y.; Khan, K.; Bernstein, M.; Balazs, A. B.; Gosnell, B. I.; Hanekom, W.; Moosa, M.-Y. S.; Lessells, R. J.; de Oliveira, T.; Sigal, A.; Ngs, S. A.; Team, C.-K., Escape of SARS-CoV-2 501Y.V2 from Neutralization by Convalescent Plasma. *Nature* **2021**.
- Ju, B.; Zhang, Q.; Ge, J.; Wang, R.; Sun, J.; Ge, X.; Yu, J.; Shan, S.; Zhou, B.; Song, S.; Tang, X.; Yu, J.; Lan, J.; Yuan, J.; Wang, H.; Zhao, J.; Zhang, S.; Wang, Y.; Shi, X.; Liu, L.; Zhao, J.; Wang, X.; Zhang, Z.; Zhang, L., Human Neutralizing Antibodies Elicited by SARS-CoV-2 Infection. *Nature* **2020**, *584* (7819), 115-119.
- Schrödinger LLC, P. *The PyMOL molecular graphics system, Versio1 1.3r1*; August, 2010.
- Abraham, M. J.; Murtola, T.; Schulz, R.; Páll, S.; Smith, J. C.; Hess, B.; Lindahl, E., GROMACS: High Performance Molecular Simulations through Multi-Level Parallelism from Laptops to Supercomputers. *SoftwareX* **2015**, *1-2*, 19-25.
- Aliev, A. E.; Kulke, M.; Khaneja, H. S.; Chudasama, V.; Sheppard, T. D.; Lanigan, R. M., Motional Timescale Predictions by Molecular Dynamics Simulations: Case Study

- using Proline and Hydroxyproline Sidechain Dynamics. *Proteins: Struct., Funct., Bioinf.* **2014**, *82* (2), 195-215.
17. Zhang, H.; Yin, C.; Jiang, Y.; van der Spoel, D., Force Field Benchmark of Amino Acids: I. Hydration and Diffusion in Different Water Models. *J. Chem. Inf. Model.* **2018**, *58* (5), 1037-1052.
18. Zhang, H.; Jiang, Y.; Cui, Z.; Yin, C., Force Field Benchmark of Amino Acids. 2. Partition Coefficients between Water and Organic Solvents. *J. Chem. Inf. Model.* **2018**, *58* (8), 1669-1681.
19. Jorgensen, W. L.; Chandrasekhar, J.; Madura, J. D.; Impey, R. W.; Klein, M. L., Comparison of Simple Potential Functions for Simulating Liquid Water. *J. Chem. Phys.* **1983**, *79* (2), 926-935.
20. Ngo, S. T.; Hung, H. M.; Truong, D. T.; Nguyen, M. T., Replica Exchange Molecular Dynamics Study of the Truncated Amyloid Beta (11-40) Trimer in Solution. *Phys. Chem. Chem. Phys.* **2017**, *19* (3), 1909-1919.
21. Tung, N. T.; Derreumaux, P.; Vu, V. V.; Nam, P. C.; Ngo, S. T., C-Terminal Plays as the Possible Nucleation of the Self-Aggregation of the S-Shape A β 11-42 Tetramer in Solution: Intensive MD Study. *ACS Omega* **2019**, *4* (6), 11066-11073.
22. Darden, T.; York, D.; Pedersen, L., Particle mesh Ewald: An N·log(N) method for Ewald sums in large systems. *J. Chem. Phys.* **1993**, *98* (12), 10089-10092.
23. Ngo, S. T.; Vu, K. B.; Bui, L. M.; Vu, V. V., Effective Estimation of Ligand-Binding Affinity Using Biased Sampling Method. *ACS Omega* **2019**, *4* (2), 3887-3893.
24. Ngo, S. T., Estimating the ligand-binding affinity via λ -dependent umbrella sampling simulations. *J. Comput Chem* **2021**, *42*, 117-123.
25. Hub, J. S.; de Groot, B. L.; van der Spoel, D., g_wham—A Free Weighted Histogram Analysis Implementation Including Robust Error and Autocorrelation Estimates. *J. Chem. Theory Comput.* **2010**, *6* (12), 3713-3720.
26. Papaleo, E.; Mereghetti, P.; Fantucci, P.; Grandori, R.; De Gioia, L., Free-Energy Landscape, Principal Component Analysis, and Structural Clustering to Identify Representative Conformations from Molecular Dynamics Simulations: The Myoglobin Case. *J. Mol. Graph. Model.* **2009**, *27* (8), 889-899.
27. Efron, B., Bootstrap Methods: Another Kook at the Jackknife. *Ann. Stat.* **1979**, *7*, 1-26.
28. Pan, A. C.; Jacobson, D.; Yatsenko, K.; Sritharan, D.; Weinreich, T. M.; Shaw, D. E., Atomic-Level Characterization of Protein-Protein Association. *Proc Natl Acad Sci U S A* **2019**, *116* (10), 4244-4249.
29. Lupardus, P. J.; Ultsch, M.; Wallweber, H.; Bir Kohli, P.; Johnson, A. R.; Eigenbrot, C., Structure of the pseudokinase-kinase domains from protein kinase TYK2 reveals a mechanism for Janus kinase (JAK) autoinhibition. *Proc. Natl. Acad. Sci. U.S.A* **2014**, *111* (22), 8025-8030.
30. Shan, Y.; Gnanasambandan, K.; Ungureanu, D.; Kim, E. T.; Hammarén, H.; Yamashita, K.; Silvennoinen, O.; Shaw, D. E.; Hubbard, S. R., Molecular basis for pseudokinase-dependent autoinhibition of JAK2 tyrosine kinase. *Nat. Struct. Mol. Biol.* **2014**, *21* (7), 579-584.
31. Tang, C.; Iwahara, J.; Clore, G. M., Visualization of Transient Encounter Complexes in Protein-Protein Association. *Nature* **2006**, *444* (7117), 383-386.
32. Frisch, C.; Fersht, A. R.; Schreiber, G., Experimental Assignment of the Structure of the Transition State for the Association of Barnase and Barstar. *J. Mol. Biol.* **2001**, *308* (1), 69-77.
33. Ngo, S. T.; Truong, D. T.; Tam, N. M.; Nguyen, M. T., EGCG Inhibits the Oligomerization of Amyloid Beta (16-22) Hexamer: Theoretical Studies. *J. Mol. Graph. Model.* **2017**, *76*, 1-10.
34. Nguyen, T. H.; Rossetti, G.; Arnesano, F.; Ippoliti, E.; Natile, G.; Carloni, P., Molecular Recognition of Platinated DNA from Chromosomal HMGB1. *J. Chem. Theor. Comput* **2014**, *10* (8), 3578-3584.

